J. Fluid Mech. (2009), *vol.* 623, *pp.* 353–374.
doi:10.1017/S0022112008005016 Printed in the United Kingdom

Energy spectra power laws and structures

P. ORLANDI†

Dipartimento di Meccanica e Aeronautica, Università La Sapienza,
Via Eudosiana 16, I-00184, Roma

(Received 19 December 2007 and in revised form 17 November 2008)

Direct numerical simulations (DNS) of two inviscid flows, the Taylor–Green flow and two orthogonal interacting Lamb dipoles, together with the DNS of forced isotropic turbulence, were performed to generate data for a comparative study. The isotropic turbulent field was considered after the transient and, in particular, when the velocity derivative skewness oscillates around -0.5. At this time, $R_\lambda \approx 257$ and a one decade wide $k^{-5/3}$ range was present in the energy spectrum. For the inviscid flows the fields were considered when a wide k^{-3} range was achieved. This power law spectral decay corresponds to infinite enstrophy and is considered one of the requirements to demonstrate that the Euler equations lead to a finite time singularity (FTS). Flow visualizations and statistics of the strain rate tensor and vorticity components in the principal axes of the strain rate tensor ($\widetilde{S}_\lambda, \widetilde{\omega}_\lambda$) were used to classify structures. The key role of the intermediate component $\widetilde{S}_2$ is demonstrated by its good correlation with enstrophy production. Filtering of the fields shows that the slope of the power law is directly connected to self-similar structures, whose radius of curvature is smaller the steeper the spectrum.

1. Introduction

A large number of natural phenomena show power law distributions; Paczuski & Bak (1999) reported several examples for which model equations are not available or have not been experimentally confirmed. In fluid dynamics, the equations describing the flow physics are known; these are derived on solid principles and have been confirmed by laboratory experiments. These equations generate energy spectra with a wide distribution in wavenumbers, whose origin is related to the nonlinearity of the Euler and Navier–Stokes equations. In real flows, a wide power law is achieved when the nonlinear terms overcome the viscous terms. This condition is verified when the Reynolds number, defined by the ratio of the two terms, is large, for instance in turbulent flows, where the Kolmogorov (1941) theory for $Re \to \infty$ predicts a $k^{-5/3}$ power law. The theory is based on the hypothesis that the energy dissipation rate $\epsilon = 2\nu \boldsymbol{S}_{ij}\boldsymbol{S}_{ji}$, with ν the kinematic viscosity and $\boldsymbol{S}_{ij}$ the strain rate tensor, remains finite for $\nu \to 0$. This hypothesis which implies that the velocity gradients increase at small scales continues to be debated. A demonstration of a limit to the rate of dissipation has been obtained recently by numerical simulations (Ishihara *et al.* 2007) for isotropic turbulence forced at low wavenumbers. At $R_\lambda > 200$ (R_λ indicates the Reynolds number based on the Taylor microscale λ) they obtained a power law one decade wide, and in addition they observed that the width of the power law

† Email address for correspondence: orlandi@kolmogorov.ing.uniroma1.it

did not increase with R_λ (Kaneda *et al.* 2003). An increase on R_λ only produced a small correction to the power law. This power law correction was previously observed by Mydlarski & Warhaft (1996). Several studies were devoted to understanding the reasons for the correction, speculating that it should be attributed to the intermittency of the rate of dissipation ϵ.

The dimensionless spectra of the Japanese team agree well with those measured in different experiments, because in laboratories also, high-*Re* isotropic turbulence is achieved by a sort of forcing at low wavenumbers, for instance in the outer region of turbulent boundary layers (Saddoughi & Veeravalli 1994) or in the centreline of round jets (Burattini, Antonia & Danaila 2005). Under these circumstances, a weak mean velocity gradient produces turbulent energy at large scales. These simulations have produced a deeper understanding of the physics of isotropic turbulence and generated energy spectra which are here used to validate the present simulations.

The aim of the present work is to investigate whether it is possible to relate the exponents of the spectra power law to the shape of vortical structures in the flow. To find this relation, the velocity field must be a solution of the Navier–Stokes equations; in fact any kind of spectra can be obtained with random phases, but these spectra do not have a physical meaning. The connection between spectra and vortical structures is facilitated by numerical simulations where all the quantities are accessible, for instance the rate of strain, the vorticity components and the pressure. It is impossible to cite the large number of papers on this topic; however, Jimenez and coworkers obtained highly interesting results for forced simulations. In their first study Jimenez *et al.* (1993) were interested in the structures with high vorticity, which they denoted as 'worms'. Previously, these structures were detected in less refined numerical simulations by Vincent & Meneguzzi (1991) and by She, Jackson & Orszag (1991). Following the flow description in the introduction of Moisy & Jimenez (2004) of turbulent flows with the inertial range followed by an exponential decay range, the large scales are immersed in a sea of small scales, and the structures can be rod- or ribbon-like. The eigenvalues $\widetilde{S}_\lambda$ of the strain rate tensor $\boldsymbol{S}_{ij}$, measured inside and around the structures, allow us to characterize the structures. The intermediate component $\widetilde{S}_2$ determines the sign of the determinant of the rate of strain tensor $\boldsymbol{R}_{\widetilde{S}} = \widetilde{S}_1\widetilde{S}_2\widetilde{S}_3$, and this determines the nature of the vortex structures. Usually the strain field is large in the regions surrounding the vortices. However, Orlandi & Carnevale (2007), describing the mechanism of vorticity amplification, observed that in the regions of vorticity amplification $\widetilde{\omega}_2^2\widetilde{S}_2$ dominates the other two components of the enstrophy production $\widetilde{\omega}_\lambda^2\widetilde{S}_\lambda$. The structures are rod-like if $\boldsymbol{R}_{\widetilde{S}} > 0$ and sheet-like if $\boldsymbol{R}_{\widetilde{S}} \leqslant 0$. From databases of different flows (forced and decaying isotropic turbulence, turbulent channels and free shear (Ashurst *et al.* 1987)), it was observed that sheet-like structures dominate and that those with $\boldsymbol{R}_{\widetilde{S}} < 0$ are unstable and contribute the most to the energy cascade.

To investigate whether the exponent of the power law in the inertial range is related to the shape of the structures, it is interesting to analyse, in addition, flows having spectra with wide power laws, without an exponential decay at high wavenumbers. Under these conditions, the small rod-like structures do not affect the structures related to the power law region. These flows can be obtained by the solution of the Euler equations with smooth initial conditions. When the spectrum with a wide power law is achieved, in a well-resolved simulation, the velocity field is saved to analyse the properties of the structures. Efficient numerical methods, as shown by Cichowlas, Debbashn & Brachet (2006), can generate flows with power spectra decaying up

to a certain wavenumber, followed by a k^2 scaling, typical of energy equipartition. However, the structures related to the k^2 range are unphysical. The inviscid simulations require smooth initial conditions, with negligible energy at small scales.

Orlandi & Carnevale (2007) performed direct numerical simulations (DNS) of the Euler equations to understand the process of vorticity amplification before the occurrence of the hypothetical finite time singularity (FTS). They claimed that, at the present time, it is impossible to have a definite and clear proof of the FTS existence for the Euler equations. They demonstrated that a model equation can be derived having a FTS. In addition they observed that, for a short time before the supposed FTS, the energy spectrum has a rather wide range with a k^{-3} power law. At high wavenumbers, the insufficient resolution produces a short range with a non-physical energy pile-up. The achievement of the k^{-3} power law was hypothesized by Kerr (1993) in a coarse simulation of interacting Gaussian dipoles (approximately 64 grid points were used to resolve the initial vortex). Spectra with $E(k) \approx k^{\gamma}$ with γ greater than -4 were observed and from these it was postulated that at a later time the asymptotic value for γ would be the order of -3.

The Orlandi & Carnevale (2007) simulations assigned as initial conditions two orthogonal Lamb dipoles (Lamb 1932) having a k^{-6} power law energy spectrum (170 grid points across each vortex), and they demonstrated that Lamb dipoles are better than Gaussian-shape vortices to study the vorticity amplification. In fact, the power law exponent $n = -6$ is preserved during the approach of the dipoles towards each other. On the other hand, during the interaction the power law is maintained with the exponent varying between $n = -6$ and $n = -3$. A proof that the initial conditions play a role in the existence of an FTS can be drawn by the results of Hou & Li (2006) and by Grafke *et al.* (2007). In the latter paper, results of different numerical schemes were compared by showing the influence of the numerical method. However, the authors claimed that 'the initial vortex tube should be chosen in such a way that vortex shedding will not pollute the vorticity growth'. The Lamb dipole has this property.

Cichowlas & Brachet (2005) assigned as the initial condition the Taylor–Green vortex to find the FTS of the Euler equations. In this flow at $t = 0$ the energy is concentrated at $k = 1.7$ and, in time, is transferred to high k. It can be speculated that a reason for the controversial arguments about the FTS, for this flow, could be related to the formation of a logarithmic decrement $\delta(t)$ of the energy at high k that varies in time. The eventual blow-up exists if $\delta(t)$ vanishes in a finite time. In the present work several resolutions, without reaching the resolution of Cichowlas & Brachet (2005) ($k_{max} = 648$), have been used to ascertain whether a spectrum with a wide power law is generated. Cichowlas & Brachet (2005) terminated the simulation before reaching a long k^{-3} range. In the present paper a simulation with $k_{max} = 256$ demonstrates that, at a certain time, a satisfactory long k^{-3} is achieved. The shape of the vortical structures and their relationship with the spectrum can then be investigated. With this resolution the smallest scales are unresolved, but the enstrophy-containing scales are not those close to k_{max}.

The present simulations were performed with a second-order finite-difference scheme, with staggered velocities. This scheme is energy-conserving in the limit of $\Delta t \to 0$. Orlandi (2000) validated this scheme for inviscid and viscous simulations. Those sceptical of the qualities of this low-order scheme and about its capability to produce results as good as those by pseudospectral methods can be convinced by the comparisons among coarse simulations of the Taylor–Green flow (Duponcheel,

Orlandi & Winckelmans 2008). For forced isotropic turbulence the same behaviour of the exponential range is established and, in addition, the energy pile-up at the high wavenumbers is smaller than found with pseudospectral methods. These comparisons demonstrate that second-order energy-conserving finite-difference schemes can be used to create databases to study the complex physics of flows with energy spectra with a wide power law range.

In order to investigate the relation between the shape of the structures in a certain range of scales in the energy spectrum, spectral filtering of the velocity field is used to analyse whether the shape is preserved in the filtered fields and to search for a self-organized critical (SOC) state. The occurrence of an SOC can be observed in several natural phenomena (Paczuski & Bak 1999), where in an ordered state every place looks like every other place. The filtering operation requires a transformation of the velocity fields from the physical to the wavenumber space, a selection of a range of wavenumbers and also setting equal to zero the amplitude of the components outside this range. A direct fast Fourier transform (FFT) of the filtered field gives the velocity components in the physical space which can be used to evaluate the statistics and to perform flow visualizations. From qualitative arguments, large differences in the statistics and in the flow structures are expected for isotropic forced turbulence, depending on the range of the spectrum considered. In addition, the weaker power law $k^{-5/3}$ decay with respect to the k^{-3}, due to the formation of the exponential range, suggests a reduction of the similarity of the structures. The constant slope over the whole spectrum in inviscid flows is typical of a self-similar cascade and of self-similar structures.

2. Numerical method and initial conditions

The Navier–Stokes and the inviscid Euler equations are solved together with the continuity equation. Since the Euler equations coincide with the Navier–Stokes equations with $\nu = 0$, the latter ones, in dimensionless form, are given as

$$\frac{\partial U_i}{\partial t} + \frac{\partial U_i U_j}{\partial x_j} = -\frac{\partial P}{\partial x_i} + \frac{1}{Re}\frac{\partial^2 U_i}{\partial x_j^2}, \quad \frac{\partial U_i}{\partial x_i} = 0, \tag{2.1}$$

where P is the dimensionless pressure. The density is assumed constant in space and time. The Reynolds number for forced turbulence is defined in § 2.3. The equations are solved in a cubic box of size 2π with the periodicity assumption in the three directions. To save computational time for the Taylor–Green and for the interacting Lamb dipoles, symmetries can be imposed. Orlandi & Carnevale (2007) demonstrated that this assumption does not affect the results. Thus in the discussion here, the full dimensions and not the true number of grid points are mentioned. Smooth initial conditions must be assigned to the Euler equations and these affect the evolution of the spectra. The results using Lamb dipoles were described by Orlandi & Carnevale (2007), and are briefly summarized here.

2.1. *Lamb dipoles*

The Lamb dipole is an exact two-dimensional form-preserving propagating solution of the Euler equations (Lamb 1932) having continuous velocity field and continuous first-spatial derivatives. In polar coordinates centred on the dipole, the vorticity distribution is

$$\begin{aligned} \omega &= -2U\kappa \tfrac{J_1(\kappa r)}{J_0(\kappa a)} \sin(\theta - \theta_0), \quad (r < a) \\ &= 0, \qquad\qquad\qquad\qquad\quad (r > a) \end{aligned} \tag{2.2}$$

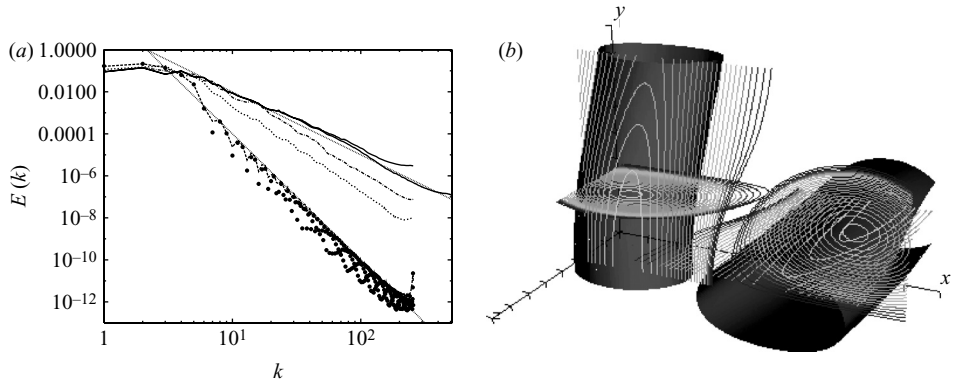

FIGURE 1. (*a*) Energy spectra: ●, $t=0$; – – – –, $t=1.00$; ·····, $t=2.00$; —·—, $t=2.50$; ———, $t=2.72$ (tick 1024^3, thin 512^3); the straight lines are k^{-6} and k^{-3} power laws; (*b*) Surface contour $|\omega|=7$ and contour lines in two orthogonal planes with $\Delta\omega=0.5$ at $t=1$.

where U, the propagation speed of the dipole, is taken as the reference velocity; a is its radius, the reference length; the time is non-dimensionalized by a/U; κ is a constant, where $\kappa a = j_1^1 \approx 3.8317$ is the first strictly positive zero of the Bessel function J_1. Equation (2.2) is a steady solution of the Euler equations in the co-moving reference frame. The dipole propagates in the direction $\theta=\theta_0$, and it can be located at any position in the computational box by changing the point of origin of the radius r.

The initial velocity fields were obtained by assigning the vorticity distribution given by (2.2) on the x_1-x_2 plane, centred at $x_1=\pi/2$ and $x_2=0$. The vorticity component ω_3 extends uniformly in the x_3 direction. The orientation of the dipole is such that it moves in the negative x_1 direction. The second dipole, with vorticity ω_2 along x_2, is centred at $x_1=-\pi/2$ and $x_3=0$. It moves in the positive x_1 direction.

In Orlandi & Carnevale (2007) the energy spectrum at $t=0$ was not shown. In this paper, focused on the energy spectra, the comparison with the initial spectrum over the period of time in which the two dipoles approach each other, before there is a large deformation, is instructive. At $t=0$, figure 1(*a*) shows small oscillations, but with a good approximation, the envelop follows a k^{-6} power law. The energy pile-up at the highest wavenumbers depends on the vorticity discontinuity at the edge of the dipoles. At $t=1$, the oscillations disappear and the k^{-6} power law is established. To give an idea about the deformations of the vorticity field of the dipoles, figure 1(*b*) shows the $|\omega|=7$ surface contour with superimposed contour lines in two orthogonal planes. In the region where the vortices interact, $|\omega|$ is distributed in a smaller area than that at $t=0$, but the shape of the vortices do not differ much. The distribution remains rather compact, and small scales are not visible. By continuing the interaction, small scales form, which generate energy spectra decaying with power laws with reduced slopes. During the time evolution, figure 1(*a*) shows that the spectra maintain a constant value of the exponent, which becomes $n=-3$ at $t=2.72$; at this time the simulations with two different resolutions produce spectra that, in large part of the range, coincide rather well. The spectra at early times have been obtained by the 512^3 resolution. The time variation of the spectra for the interacting Lamb dipoles is different from that for the Taylor–Green flow, which is described in the next section.

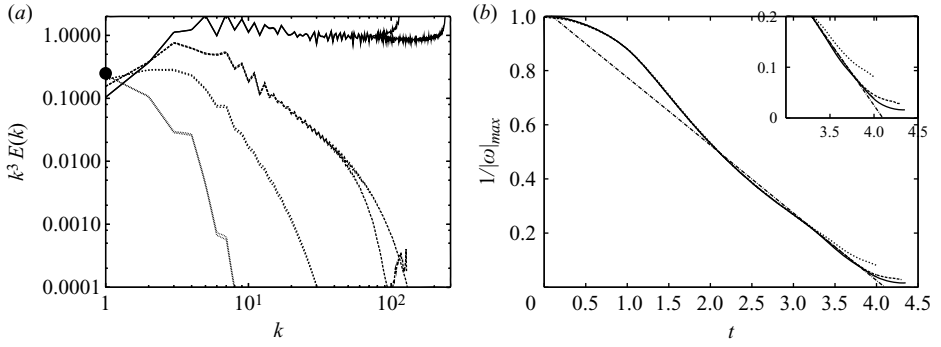

FIGURE 2. (a) Compensated energy spectra ($k^3E(k)$): ●, $t=0$; — - —, $t=1$; ·····, $t=2$; - - - -, $t=3$; ———, $t=4.27$ (thick 512^3, thin 256^3); (b) inverse of maximum vorticity time evolution: ———, 512^3; - - - -, 256^3; ·····, 96^3; straight line, $0.25(4.1-t)$.

2.2. *Taylor–Green flow*

For this flow the initial conditions are given by

$$u_1 = U\sin(x_1)\cos(x_2)\cos(x_3),$$
$$u_2 = -U\cos(x_1)\sin(x_2)\cos(x_3),$$
$$u_3 = 0, \tag{2.3}$$

which give an energy spectrum with only one non-zero mode $E(k=1.7)$. As for the Lamb dipoles the cubic box has a size 2π, the reference velocity is $U=1$ and the Euler equations are integrated in time with the third-order Runge–Kutta time-stepping scheme, which is more accurate than that of Adams–Bashfort, as shown in Duponcheel *et al.* (2008). The time evolution of the compensated spectra ($k^3E(k)$) in figure 2(a) shows, in the transient, the formation of logarithmic decrements of the energy at high k and a smaller extension of the power law than that for the Lamb dipoles. By triadic interactions, the energy content initially at $k=1.7$ is transferred to high wavenumbers. This process is produced by the vortex tilting and stretching terms in the vorticity transport equations. During the evolution, Cichowlas & Brachet (2005) found that the spectra can be fitted to $E(k)\approx k^{\gamma(t)}\mathrm{e}^{-2\delta(t)k}$, and they presented the time evolution of $\gamma(t)$ and $\delta(t)$. Here the interest is to find whether $\gamma=-3$ can be achieved, and indeed figure 2(a) does show that at $t=4.27$ a satisfactorily wide k^{-3} range is established. For the interacting Lamb dipoles, figure 1(a) shows that in time the spectra have power laws extending over the whole range. For the Taylor–Green flow the loss of self-similarity perhaps is one of the reasons of the controversy in the demonstration of the hypothetical FTS. The spectra in figure 2(a) evaluated by the simulation with the 512^3 grid are compared with the spectra by a 256^3 grid. The comparison shows that the scales in the k^{-3} range are well resolved except for a short range close to k_{max}. Better resolution should increase the length of the k^{-3} range.

In this paper, the question of the existence of an FTS is not discussed; however, the vorticity amplification is analysed by looking at the time evolution of $1/|\omega|_{max}$. As in Cichowlas & Brachet (2005), without reaching their finest resolution, several simulations produced the results as represented in figure 2(b). A 96^3 grid gives inaccurate results, but those with a 256^3 grid do not differ much from those with a 512^3 grid. The $1/|\omega|_{max}\approx(t_s-t)$ is well fit between $t=3$ and $t=3.8$. To extend the fit, at $t>4$, a huge number of grid points is required. The enstrophy-containing

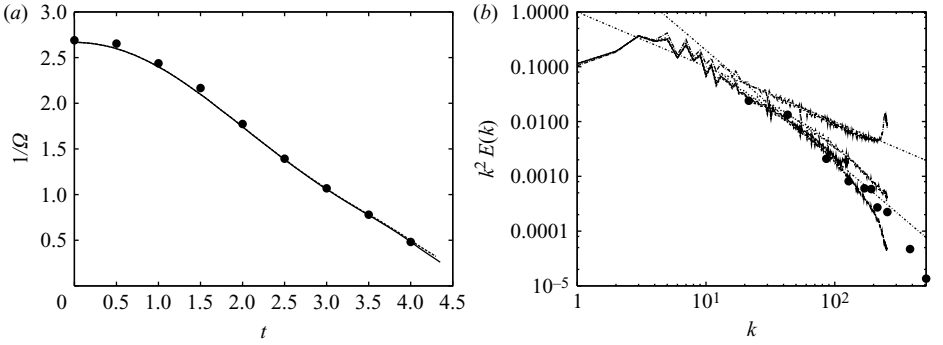

FIGURE 3. (*a*) Inverse of enstrophy ($\Omega = \langle \omega_i^2 \rangle / 2$) time evolution: ——, 512^3; – – – –, 256^3; (*b*) enstrophy spectra at $t = 3.96$ (– – – –), $t = 4.00$ (——), $t = 4.06$ (·····), $t = 4.27$ (— – —); ● Cichowlas & Brachet (2005) in (*b*) indicates the spectrum at $t = 4$ obtained by their figure 2.

structures, for spectra decaying as k^{-3}, are not linked to the highest wavenumbers. The results in figure 2(*b*) show that a vorticity amplification similar to that for the Lamb dipoles occurs, and accordingly a k^{-3} power law spectrum is achieved at a time close to t_s. The compensated energy spectra ($k^3 E(k)$) in figure 2(*a*) at $t = 4.27$ have a constant value equal to 1 between $k = 3$ and $k = 200$, and the enstrophy-containing range extends between $k = 2$ and $k = 10$ (figure 3*b*).

The present results seem to contradict those obtained by Cichowlas & Brachet (2005). In fact, in their figure 3, n never reaches a value equal to -3. Therefore, it is necessary to compare the two simulations. From their figure 1, the values of the enstrophy $\Omega(t)$ have been evaluated and plotted as $1/\Omega$ in figure 3(*a*). This shows very good agreement between their enstrophy amplification and ours, implying that their lack of resolution affects the high-wavenumber spectra and does not affect the enstrophy. Cichowlas & Brachet (2005), by stopping the simulations at $t = 4$, could not observe a k^{-3} range. In figure 3 the enstrophy spectra of the present simulations at $t = 4.00$ compare rather well with that of Cichowlas & Brachet (2005) and, in addition, show that in a short period after $t = 4.00$, our simulations achieve a k^{-3} range. The small pile-up at $t = 4.27$ indicates that the vorticity field is satisfactorily resolved.

2.3. *Forced isotropic turbulence*

For this flow the initial conditions are unimportant; instead it is necessary to explain the forcing at large scales which maintain constant the turbulent kinetic energy. The present forcing is different from the negative viscosity coefficient for $|k| < 2.5$ used by Jimenez *et al.* (1993), or the solenoidal random forcing at small scales by Gotoh, Fukayama & Nakano (2002). Other ways of forcing at large scale were used, some of which are described by Alvelius (1999), and there is the possibility that a way similar to the present one was applied. However, despite the differences in the time evolution, different simulations should give the same stationary value for the velocity derivative skewness.

To maintain constant the r.m.s. of each velocity component, at each third sub-step of the third-order Runge–Kutta time-stepping scheme, when the non-solenoidal velocity field is evaluated, the dissipated energy is injected at large scales. The inverse FFT furnishes the velocity in k space by fixing a wavenumber k_F (here $k_F = 3$), and the energy content for each velocity component ($\Sigma_{k<k_F} E_i(k)$) is evaluated. At all wavenumbers, the energy lost for viscous effects is injected at small k by multiplying

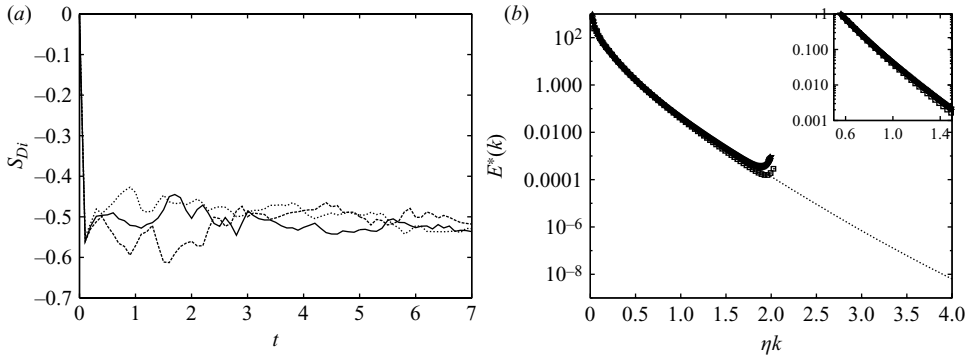

FIGURE 4. (*a*) Time evolution of the three velocity derivative skewness: ———, $i=1$; – – – –, $i=2$; ·····, $i=3$ for $Re=1568$ and a 512^3 grid; (*b*) Kolmogorov spectra, with an enlargement near $k^*=1$: lines finite difference – – – –, $R_\lambda=127$ (256^3); ·····, $R_\lambda=109$ (512^3), ———, $R_\lambda=252$ (512^3); symbols pseudospectral: □, $R_\lambda=62$ (128^3); ○, $R_\lambda=95$ (256^3); △, $R_\lambda=142$ (384^3); ∇, $R_\lambda=168$ (512^3) (the data are in Jimenez *et al.* (1993)).

the amplitude of each component at wavenumbers $k<k_F$, for $F_i=\sqrt{(1+Q_i)}$ (i indicates the velocity component), where $Q_i=(q^2/3-\Sigma E_i(k))/\Sigma_{k<k_F}E_i(k)$. With this operation the energy spectrum for $k>k_F$ does not change. The r.m.s. for each velocity component remains identically equal to 1 (the value assumed as reference velocity). Figure 4(*a*) shows that the three velocity derivative skewness,

$$S_{Di}=\frac{\left\langle \left(\dfrac{\partial u_i}{\partial x_i}\right)^3 \right\rangle}{\left\langle \left(\dfrac{\partial u_i}{\partial x_i}\right)^2 \right\rangle^{3/2}}, \tag{2.4}$$

starting from the value of 0, characteristic of the random phases assigned at $t=0$, grow in time and finally oscillate around -0.5, which is expected for isotropic turbulence at high Re. This figure is similar to figure 10 in Alvelius (1999), obtained at three Re numbers smaller than that used here. Figure 4(*a*) shows that the statistical steady state is reached at an earlier time.

The Reynolds number is $Re=u'L/\nu$, with $u'^2=2/3\int E(k)\mathrm{d}k$. The size of the computational domain is $2\pi L$. To perform a true DNS it is necessary to assume a value of the kinematic viscosity ν leading to a Kolmogorov length scale $\eta=(\nu^3/\epsilon)^{1/4}$, with $\epsilon=2\nu\int k^2E(k)\mathrm{d}k$ the rate of energy dissipation, greater than the grid size Δx_i. Three simulations were performed to investigate whether the present numerical scheme predicts a satisfactory exponential decay of the energy dissipation range. At $t=4$, with $Re=294$ and a 512^3 grid, $R_\lambda=u'\lambda/\nu$ was equal to 109, $\lambda=\sqrt{(15\nu u'^2/\epsilon)}$ being the Taylor microscale. At this time, approximately one eddy turnover time, $\eta k_{max}=4.5$, implying a good resolution of the small scales. To have large structures with the same grid, the assumption of $Re=1568$, and consequently $R_\lambda=257$, leads to $\eta k_{max}=1.3$ at $t=7$. This is a quite high R_λ with a short inertial range. In literature, energy spectra by pseudospectral simulations with different resolutions (Jimenez *et al.* 1993; also in AGARD AR-345 1998) allow to make comparisons. Figure 4(*b*) displays that second-order finite differences produce dimensionless spectra ($E^*(k^*)=E(k)/(\nu^5\epsilon)^{1/4}$ and $k^*=k\eta$) with a negligible energy pile-up at the highest k, with respect to that by pseudospectral simulations. To investigate whether the negligible pile-up of the finite difference could depend on the resolution, a further 256^3 simulation with $Re=400$

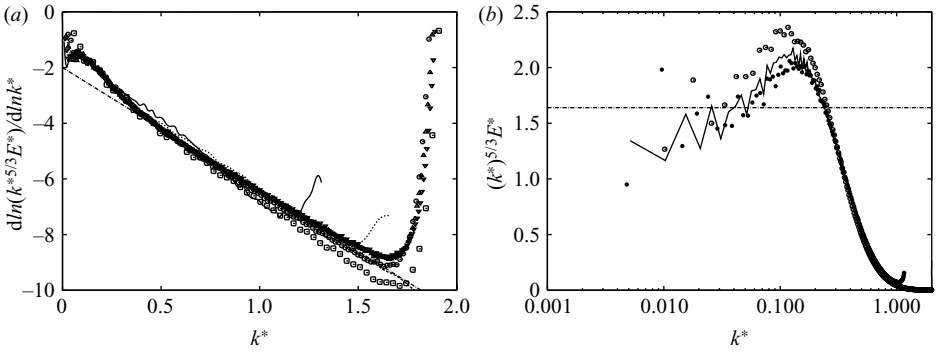

FIGURE 5. (*a*) Differentiated compensated spectra legend as figure 4(*b*) the fitted line is obtained with ····· $C=2$, $\beta=4.4$, (*b*) Kolmogorov compensated spectra for ○ Jimenez *et al.* (1993) at $R_\lambda=168$, ● Gotoh *et al.* (2002) at $R_\lambda=284$, ——— present at $R_\lambda=257$.

($R_\lambda=127$ and $\eta k_{max}=1.66$) was performed. Also in this case the spectra do not show any significant pile-up.

An analytical expression for $E^*(k^*)$ is often used, and the most accepted is

$$E^*(k^*)=Ck^{*\alpha}\exp(-\beta k^{*n}), \tag{2.5}$$

where C, α, β and n are constants. As resumed by Ishihara *et al.* (2005) a linearization of the small-scale dynamics leads to $n=2$, but spectral closures, DNS and experiments suggest that $n=1$ is more appropriate; in addition, they claimed that it seems unlikely that it will be possible to give a rigorous theoretical derivation of the form of the spectrum in the dissipation range. Since it is difficult to measure the spectrum at high wavenumbers, as the signal level is so weak as compared to the background noise at these scales, the only way is to use the results of DNS to get the values of the constants. The plots of $d\ln\hat{E}/d\ln k^*$, with $\hat{E}=k^{*5/3}E^*$ (around $k^*=1$), are useful to validate the results in the exponential range. The data in figure 4(*b*) generate the curves of $d\ln\hat{E}/d\ln k^*$ shown in figure 5(*a*), which, for both numerical methods, are fitted by (2.5) with $C=2$ and $\beta=4.4$. This figure shows that despite the differences in energy pile-up at high k, there is no influence of the numerical method. The absence of differences near $k^*=1$ for forced isotropic turbulence confirms the message from Grafke *et al.* (2007) that 'the flow has to be resolved and this is more important than the order of the scheme'.

The interest in the present paper is focused to analyse the shape of the structures contributing to the energy spectrum in the inertial range and in the range of wavenumbers where the bump in figure 5(*b*) occurs. These are the enstrophy-containing structures. Figure 5(*b*) shows the compensated Kolmogorov spectra ($\hat{E}(k^*)$) by the present simulation at $R_\lambda=257$, the Jimenez *et al.* (1993) at $R_\lambda=168$ and the Gotoh *et al.* (2002) at $R_\lambda=284$, obtained with different forcing and numerical methods. The results show the formation of a short inertial range; the differences at the largest scales depend on the different ways of forcing.

Before discussing the link between structures and power laws, a further validation of the present simulations is obtained by comparing the values of the normalized mean energy dissipation rate $D=\epsilon L_I/u'^3$, with $L_I=\pi\int k^{-1}E(k)\mathrm{d}k/2u'^2$ the integral length scale. For $R_\lambda=127, 105$ and 257, the present values of D 0.39, 0.37 and 0.35 are close to those obtained by Ishihara *et al.* (2007). The value of L_I in the present simulation is approximately 1.4, indicating that the box size does not affect the results.

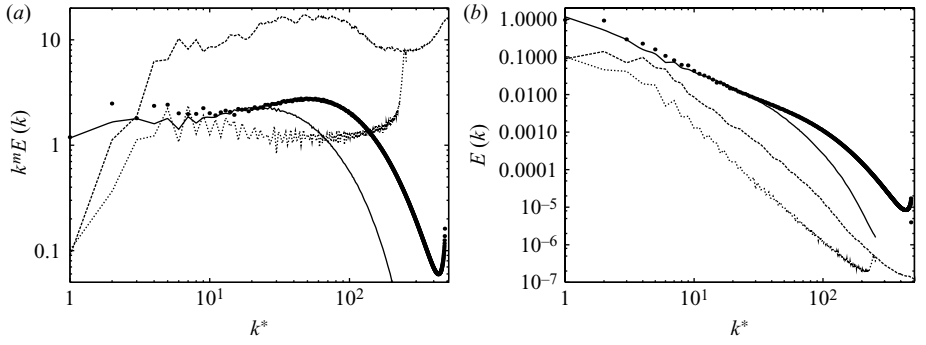

FIGURE 6. (*a*) Compensated spectra: – – – –, Lamb dipoles; ·····, Taylor–Green ($m = 3$); ———, forced turbulence; ●, Gotoh *et al.* (2002) ($m = 5/3$); (*b*) Not-compensated spectra.

3. Spectra and structures

To summarize, three fields have been considered, two without viscosity and one with viscosity. The comparison between viscous and inviscid simulations allows to investigate whether a connection between the turbulent structures, contributing to the inertial range and those emerging from inviscid interactions, does exist. In the latter flow the small scales related to the viscosity do not form, and then the enstrophy-containing structures generated by the nonlinear term are not contaminated.

The inviscid fields evolving from smooth initial conditions are taken after a stage of large vorticity amplification. Simulations with infinite resolution at a certain time t_s should lead to energy spectra with a k^{-3} power law, corresponding to infinite enstrophy. A finite number of degrees of freedom produces unphysical small scales with an energy pile-up at the highest wavenumbers. A non-dissipative numerical method can integrate the inviscid equations for $t > t_s$ by reaching energy equipartition with $E \approx k^2$, but the associated structures are unphysical. To have structures of physical meaning the simulations were stopped when the widest k^{-3} range was observed. The small energy pile-up at high wavenumbers has an enstrophy k^2E negligible with respect to that of the energy-containing scales. The insufficient resolution thus produces small oscillations in the low-level vorticity contours. However, the velocity contours are smooth, and the pressure contours even smoother.

A viscous simulation of forced isotropic turbulence furnishes the third field with a $k^{-5/3}$ spectrum one decade wide. It is important to recall that high resolution is needed to generate the dissipation range. This is the requirement for a true DNS. Figure 6(*a*) shows that the three compensated spectra $k^m E(k)$ have a long power law ($m = 3$ for inviscid, $m = 5/3$ for viscous). Figure 6(*a*) shows that in the inertial range, the present compensated spectrum at $R_\lambda = 257$ (not in Kolmogorov variables) agrees with that by Gotoh *et al.* (2002) with a 1024^3 resolution. The difference in the large scales for $k < 10$ depends on the different ways of forcing. The non-compensated spectra in figure 6(*b*) show clearly that the pile-up has energy negligible with respect to that at large scales.

3.1. *Structures identification*

3.1.1. *Inviscid flows*

Accurate numerical simulations promoted the interest to find methods to identify vortical structures. For instance Horiuti & Takagi (2005) reported eduction methods for sheet- and rod-like structures; the latter structures affect the inertial range. In

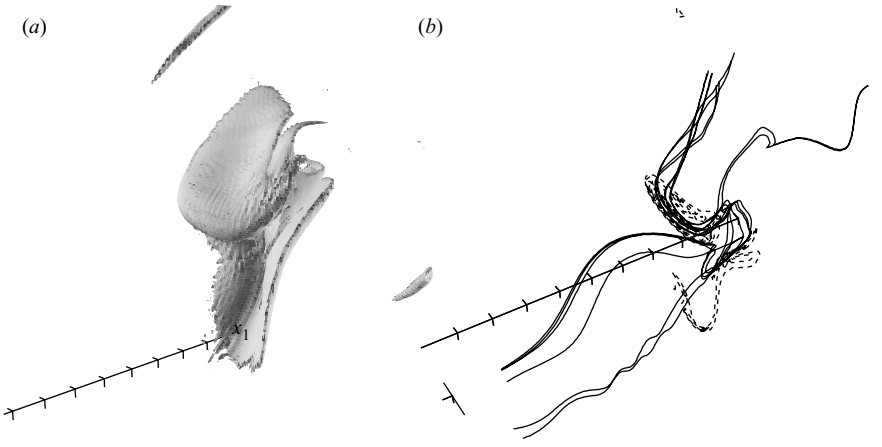

FIGURE 7. (*a*) $|\omega| = 80$ surface contour for the Lamb dipoles; (*b*) ——, vortex lines originated near the location of $|\omega|_{max} = 550$ and – – – –, $|\omega|$ contours with $\Delta|\omega| = 50$ in the $x_2 - x_3$ plane passing through the point of $|\omega|_{max}$.

this paper the vortical structures are qualitatively identified by $|\omega|$ surface contours. Work is in progress to give quantitative measures of curvature of vortex lines and curvature of three-dimensional surfaces of $|\omega|$. In the flow visualizations, different values of $|\omega|$ are assumed; for inviscid flows depend on the vorticity magnitude at $t = 0$, and on the Reynolds number for viscous flows. For the Taylor–Green flow the amplification is $|\omega|_{max}(t = 4.27)/|\omega|_{max}(t = 0) = 41$, for the Lamb dipoles it is $|\omega|_{max}(t = 2.72)/|\omega|_{max}(t = 0) = 47$ and for forced isotropic turbulence at $t = 7$, $|\omega|_{max} = 250$. For the Lamb dipoles the surface contour of $|\omega| = 80$ in figure 7(*a*) shows the formation of two thin vorticity layers of lens shape. The qualitative impression of the curvature of vortex lines is shown in figure 7(*b*) by nine vortex lines originating from nine points around the location of $|\omega|_{max}$. The dashed lines depict contours of $|\omega|$ in a $x_2 - x_3$ plane passing through the point with $|\omega|_{max}$. This figure shows the occurrence of large values of curvature.

The amplification for the Taylor–Green flow leads to the formation of two thin vortex-sheet structures (depicted by a surface contour of $|\omega| = 10$) near the symmetry planes (figure 8*a* has the x_2-axis inverted for a better view); one is straight and long, and the other short. The latter, in the symmetry plane, has $|\omega|$ contours with a small curvature radius near the location of $|\omega|_{max}$. The contours of $|\omega|$ in the symmetry plane are shown in figure 8(*b*) together with vortex lines originating from points near the location of $|\omega|_{max}$. The vortex lines with small curvature radii lie between the two vortex sheets, having the common feature to be thin and to extend for a short distance in the x_2 direction. From figures 7(*a*) and 8(*a*), it can be estimated that the greatest enstrophy contribution comes from the curved structure with an approximate size of 16^3 grid points, corresponding to the peak of $k^2E(k)$ at $k = 8$.

3.1.2. *Isotropic turbulence*

The viscous simulations generate a large variety of structures (figure 9), with size uniformly distributed. This behaviour explains why the inertial range of the spectrum has a power law less steep than that for the isolated inviscid structures. The extension of the power law in the entire range is a manifestation of self-similar structures at different scales, with decreasing energy and enstrophy, implying a local energy transfer between eddies of similar size. For isotropic turbulence the local transfer

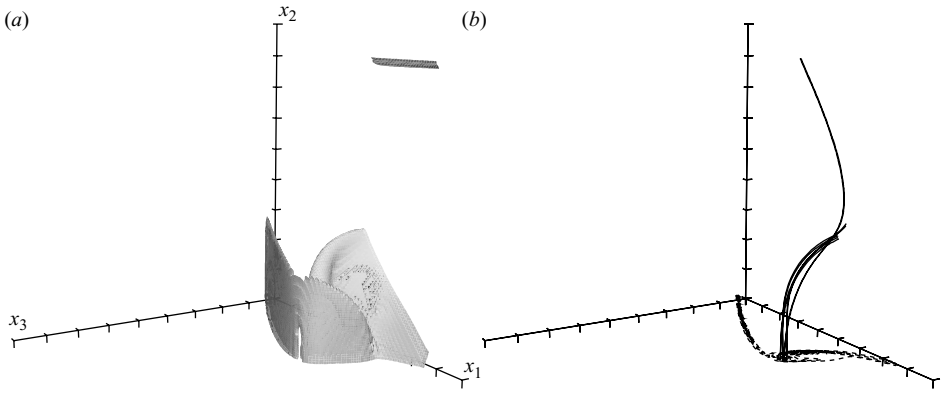

FIGURE 8. (*a*) $|\omega|$ surface contour for Taylor–Green $|\omega| = 10$ (*b*) ——, vortex lines originated near the location of $|\omega|_{max} = 80$ and – – – –, $|\omega|$ contours with $\Delta|\omega| = 10$ in the $x_1 - x_3$ plane passing through the point of $|\omega|_{max}$.

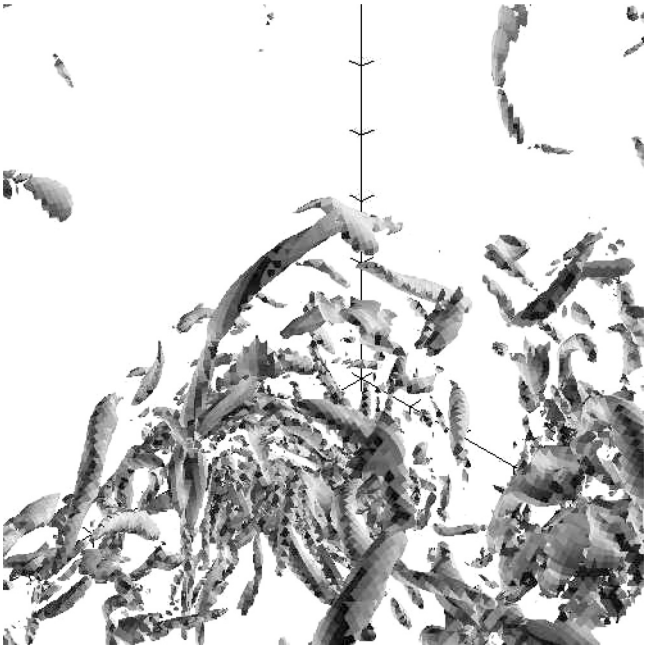

FIGURE 9. $|\omega|$ surface contour for forced isotropic turbulence $|\omega| = 80$.

was postulated by analysing the triadic interactions in spectral closures by Crocco & Orlandi (1985), and later on verified by DNS (Domaradzki & Rogallo 1990). In physical space it is rather difficult to understand how energy is transferred to smaller scales; however, an approximate idea is obtained by filtering the velocity field. If this operation shows that the shape of the structures does not change and reduces in size, it can be postulated that energy is transferred to structures of similar shape, as it will be demonstrated later on. The filtering operation consists of the application of an inverse FFT to have the velocity components in wavenumber space, by setting $U_i(k_1, k_2, k_3) = 0$ for $k_L < k < k_U$. A direct FFT of this field gives the velocity fields in physical space.

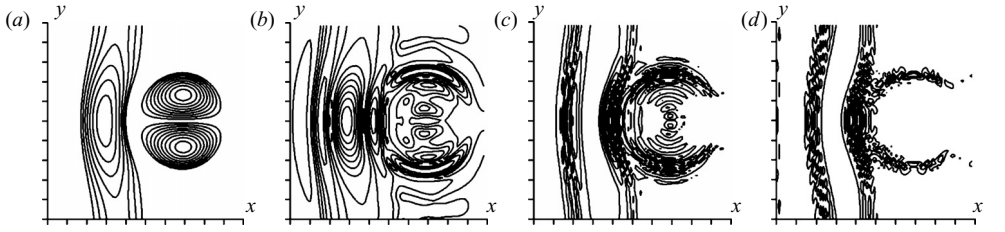

FIGURE 10. $\widehat{\omega} = |\omega|/|\omega|_{max}$ contours for the filtered Lamb dipoles at $t = 1$ with (*a*) $k_L = 0$, $k_U = 256$, $|\omega|_{max} = 11.94$; (*b*) $k_L = 6$, $k_U = 20$, $|\omega|_{max} = 2.76$; (*c*) $k_L = 20$, $k_U = 60$, $|\omega|_{max} = 0.91$; (*d*) $k_L = 60$, $k_U = 120$, $|\omega|_{max} = 0.23$, $\Delta\widehat{\omega} = .1$ Here $x = x_1$, $y = x_2$.

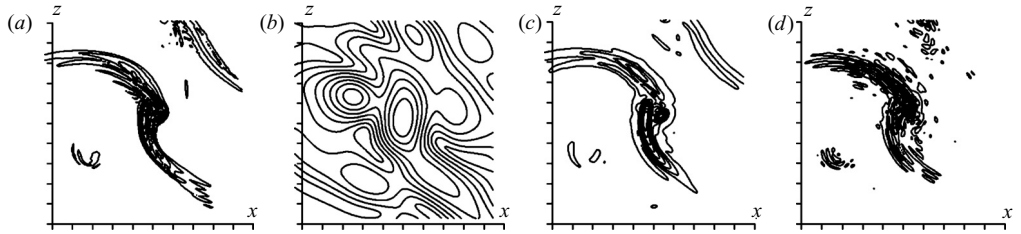

FIGURE 11. $\widehat{\omega} = |\omega|/|\omega|_{max}$ contours for the filtered Lamb dipoles with (*a*) $k_L = 0$, $k_U = 500$, $|\omega|_{max} = 565.8$; (*b*) $k_L = 6$, $k_U = 20$, $|\omega|_{max} = 48.8$; (*c*) $k_L = 20$, $k_U = 110$, $|\omega|_{max} = 411.7$; (*d*) $k_L = 110$, $k_U = 200$, $|\omega|_{max} = 224.7$, $\Delta\widehat{\omega} = 1$. Here $x = x_1$, $z = x_3$.

3.2. *Structure similarity*

To see the shape of the resulting structure on filtering a velocity field associated to simple vortical structures, the field of the two interacting Lamb dipoles at $t = 1$ has been considered. The spectrum and the structures in figure 1 show that the vorticity amplification is not initiated, and thus the 512^3 resolution is used for the analysis. A different value of $|\omega|_{max}$ is found at each filtering level, and the contours of $\widehat{\omega} = |\omega|/|\omega|_{max}$ are plotted. The dipole deformations can be observed in a $x_1 - x_2$ plane cutting the two dipoles. Figure 10(*a*) obtained with the unfiltered field shows a mild deformation, which does not substantially change with $k_L = 0$ and $k_U = 6$. With $k_L = 6$ and $k_U = 20$, thin curved vortical patches appear in the regions adjacent to those where the vorticity in figure 10(*a*) is located. Figures 10(*c*) and 10(*d*) emphasize the reduction in size of the patches by filtering at high wavenumbers. Figures 10(*b–d*) give a qualitative idea of the structure similarity related to the k^{-6} power law of the energy spectrum between $k_L = 6$ and $k_U = 120$ (figure 1*a*). A more quantitative demonstration of the self-similarity is given by one-dimensional profiles of $\widehat{\omega}$. These plots are shown at $t = 2.72$ when the highest vorticity amplification occurs.

Figure 6 exhibits three well-defined k^{-3} ranges, between $k_L = 6$ and $k_U = 200$, after a sufficient long period of vorticity amplification. Figure 11 demonstrates, through contour plots of $|\omega|/|\omega|_{max}$ in $x_1 - x_3$ planes passing through the point of $|\omega|_{max}$, that enstrophy and energy (with similar figures not presented) are located in curved layers thinner as higher the filtering interval is. The plots with $k_L = 200$ and $k_U = 350$ are not given because the contours are affected by the scales not fully resolved. The size of the structures does not decrease as fast as those in figure 10, and this explains why the energy spectrum has a weaker power law (k^{-3} instead of k^{-6}).

Also for the Taylor–Green flow, figure 6 shows a k^{-3} between $k_L = 50$ and $k_U = 150$ and figure 8(*a*) depicts ribbon-like thin vorticity layers near the symmetry plane.

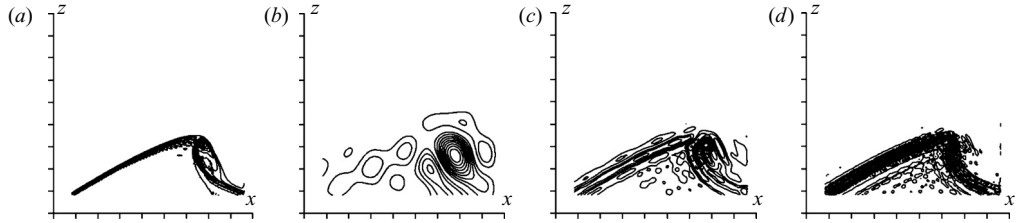

FIGURE 12. $\widehat{\omega} = |\omega|/|\omega|_{max}$ contours for the filtered Taylor–Green with (*a*) $k_L = 0$, $k_U = 250$, $|\omega|_{max} = 41.6$; (*b*) $k_L = 6$, $k_U = 20$, $|\omega|_{max} = 13.8$; (*c*) $k_L = 20$, $k_U = 60$, $|\omega|_{max} = 20.7$; (*d*) $k_L = 60$, $k_U = 120$, $|\omega|_{max} = 17.0$, $\Delta\widehat{\omega} = 1$. Here $x = x_1$, $z = x_3$.

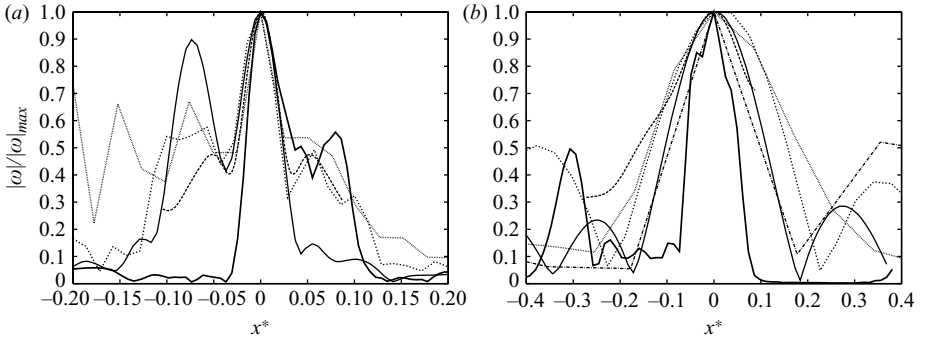

FIGURE 13. One-dimensional profiles of normalized $|\omega|$ versus normalized x_1 at the point of $|\omega|_{max}$, for the unfiltered field (tick solid line) and for the filtered fields; (*a*) Lamb dipoles: – – – –, $k_M = 13$; ———, $k_M = 65$; ·····, $k_M = 155$; ·····, $k_M = 275$; (*b*) Taylor–Green: – – – –, $k_M = 3$; ———, $k_M = 13$; ·····, $k_M = 40$; ·····, $k_M = 90$; — – —, $k_M = 188$.

Visualizations in an $x_1 - x_3$ plane at $x_2 = 0$ present the structures emerging from the filtering operation. Figure 12(*b*) shows that at small k the enstrophy is concentrated in two fat regions, which at higher wavenumbers become thin; one has a greater curvature in the region where $|\omega|_{max}$ is localized (figure 12*c*). Figure 12(*d*) qualitatively indicates that energy is transferred to smaller scales. The figure with $k_L = 120$ and $k_U = 250$ is not shown because the insufficient resolution produces large oscillations in the $\widehat{\omega}$ contours. However, also in this range of wavenumbers, the most energetic scales have a shape similar to that in figure 12(*a*). The plots of vorticity norm display regions of high enstrophy, which coincide with the energy-containing scales. This assertion has been verified by plots of velocity norm. In conclusion, the filtering operation emphasizes that at all filtered scales, $|\omega|$ is concentrated in spiral regions with high curvature; in these regions the vorticity is amplified. In fact, it has been observed that at each filtering level in the symmetry plane, the thin straight vorticity layer, on the left of figure 12(*a*), has contour levels $\widehat{\omega} < 0.75$.

The occurrence of self-similar structures in the k^{-3} range cannot be clearly demonstrated by the planar view in figures 11 and 12, which is more quantitatively emphasized by one-dimensional profiles of $\widehat{\omega}$ crossing the location of $|\omega|_{max}$. A self-similarity does exist when the size of the structures scale with the interval of wavenumbers used for filtering. The comparison, in the one-dimensional plots, requires the normalization of $|\omega|$ by the $|\omega|_{max}$ at each filter level. The origin of the coordinate $x = x_1 - x_{1M}$ coincides with the point x_{1M} where $|\omega|_{max}$ is located. In figure 13 the unfiltered profile and that with $k_L = 20$ are plotted versus $x^* = x$, for the

other filtered fields $x^* = x\ k_M/k_{M3}$, where $k_M = (k_L + k_U)/2$ and k_{M3} is the averaged wavenumber with $k_L = 20$. For the Lamb dipoles, figure 13(a) shows a collapse of all curves around $x^* = 0$, implying that at each filter level, the most energetic structures are self-similar. The worse collapse for the Taylor–Green flow could be attributed to the lack of self-similarity during the evolution. This is a further indication that the flow generated by the interaction of Lamb dipoles should be useful to understand the physical mechanism leading to an FTS.

The filtering of the isotropic forced turbulent flow gives rise to different shapes of vorticity patches, depending on the values of k_L and k_U. For this flow the qualitative picture is achieved by three-dimensional visualizations. The shape and the size of the vortical patches are better appreciated by surface contours of $|\omega|$ in a small section of the entire computational box. Figure 9 displays very elongated tubular structures with a small core radius and a small number of ribbon-like structures. Vincent & Meneguzzi (1991) were interested to detect tubular structures and observed that these contribute to the entire energy spectrum. By filtering the field they produced a figure (figure 17, p. 16), claiming the formation of helical structures. Holm & Kerr (2007) considered turbulent fields, with a short $k^{-5/3}$ range, evolving from smooth initial conditions, and they observed in the first stage the formation of vortex sheets, which later on became vortex tubes. Horiuti & Fujisawa (2008) at $R_\lambda \approx 75$ showed that vortex sheets are entrained by vortex tubes and form spiral vortices. Here the interest is to isolate different parts of the spectra and to detect, by flow visualizations of $|\omega|$ surface contours, the structures contributing to the part of the spectrum considered. With $k_L = 6$ and $k_U = 20$ the very large scales (where the forcing is applied ($k < 3$)) and the small scales are discarded. This interval of wavenumbers corresponds to the range where the compensated spectra ($k^{5/3}E(k)$) in figure 6(a) is constant. Figure 14(a) shows the vorticity patches detected in this region; these structures are the unstable ribbon-like structures which, by mutual interaction, transfer energy to small scales.

The structures are different by filtering at high k, and in particular in the region where the bump in the compensated spectrum (figure 6a and emphasized in figure 5b) occurs. Few ribbon-like structures in figure 14(b) are encircled by a large number of rod-like structures. To understand whether the large structures in figure 14(a) or the small ones in figure 14(b) contribute to the structures in figure 9, $|\omega|$ contour plots in a $x_1 - x_3$ plane may help. In figures 15(a) and 15(b) the shaded contours of $|\omega|$ obtained by the unfiltered field show that intense vorticity is concentrated in a circular region of small size. In figure 15(a) the thick solid contour lines, corresponding to $|\omega| = 20$ in figure 14(a), show that often the large scales encircle the intense tubular structures; this is an evidence of the local energy transfer from large to small scales. In figure 15(b) the solid lines corresponding to $|\omega| = 33.68$ in figure 14(b) depict a good correspondence between the structures. From this observation it can be asserted that in isotropic turbulence the intense vorticity structures are due to the part of the spectra near the end of the inertial range. The comparison between viscous and inviscid visualizations shows that the viscosity destroys the structure self-similarity produced by the inviscid vortices interaction. It seems correct to conclude that the bump in the compensated spectra (the bottle-neck) observed also in laboratory experiments (Saddoughi & Veeravalli 1994) is due to the roll-up of unstable ribbon-like structures which form rod-like structures. By filtering at higher wavenumbers, at the beginning of the exponential range, smaller rod-like structures appear in figure 14(c) than those in figure 14(b); some degree of anisotropy persists, which disappears in figure 14(d) with $k_L = 120$ ($k_L^* = 0.5$) and $k_U = 240$ ($k_U^* = 1$). In this figure the surface level has been reduced to $\widehat{\omega} = 0.15$ because of the low energy content for $k^* = O(1)$.

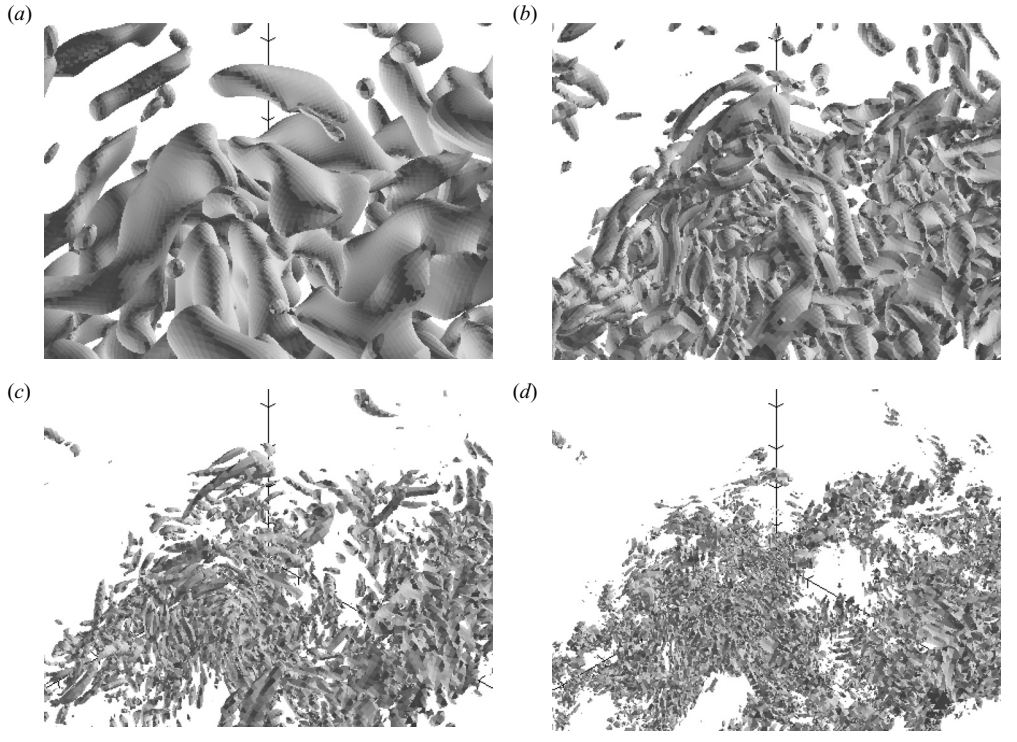

FIGURE 14. $\widehat{\omega}$ surface contour for forced isotropic turbulence: (*a*) $k_L =$, 6, $k_U = 30$; (*b*) $k_L = 30$, $k_U = 70$; (*c*) $k_L = 70$, $k_U = 120$; (*d*) $k_L = 120$, $k_U = 240$; in (*a*)–(*c*) $\widehat{\omega} = 0.3$, and in (*d*) $\widehat{\omega} = 0.15$.

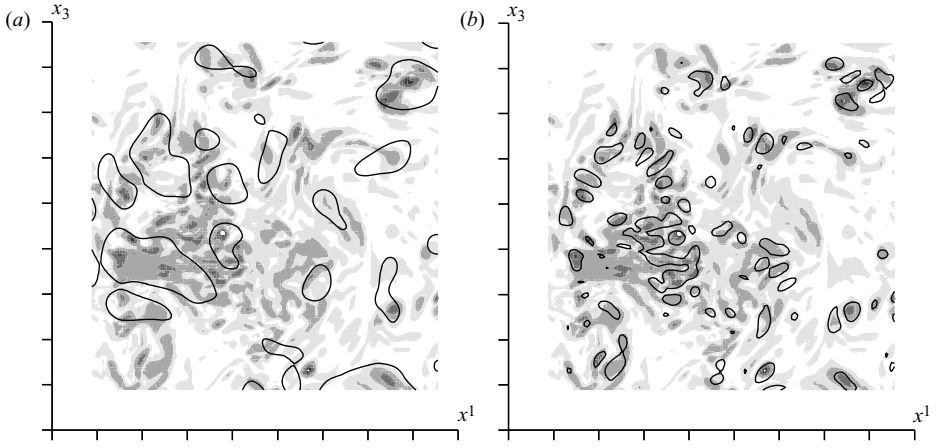

FIGURE 15. Shaded contours of $|\omega|$ considering the full spectrum: (*a*) solid line (that in figure 14(*a*) with $|\omega| = 20$), (*b*) solid line (that in figure 14(*b*) with $|\omega| = 33.68$).

3.3. *Probability density function of* $|\omega|$

The $|\omega|$ visualizations for viscous and inviscid simulations present a qualitative picture. A satisfactory comprehension of the differences or of the similarities between viscous and inviscid flows is obtained by a more quantitative information drawn by the p.d.f. of $\sigma = |\omega|/\langle\omega^2/2\rangle^{1/2}$. The p.d.f. have been evaluated by considering all the points.

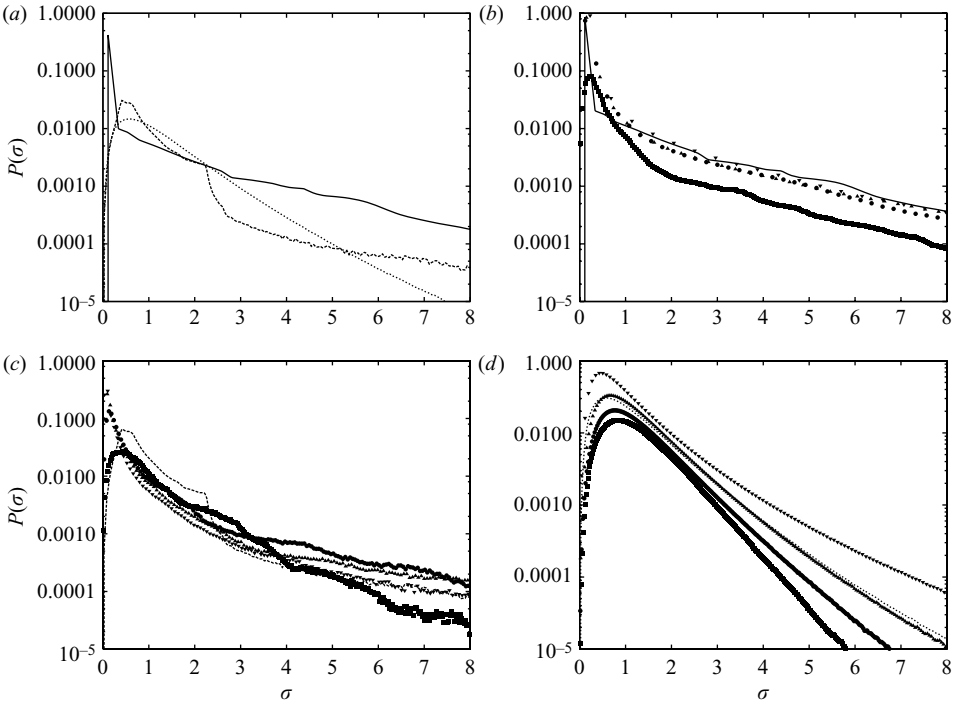

FIGURE 16. The p.d.f. of $\sigma = |\omega|/\langle\omega^2/2\rangle^{1/2}$ for (a) comparison of the three flows (——, Lamb; – – – –, Taylor–Green; and ·····, forced turbulence); (b) Lamb —— full: ■ $k_L = 6$ and $k_U = 20$, ● $k_L = 20$ and $k_U = 110$, ▲ $k_L = 110$ and $k_U = 200$, ▼ $k_L = 120$ and $k_U = 250$; (c) Taylor–Green – – – – full: ■ $k_L = 6$ and $k_U = 20$, ● $k_L = 20$ and $k_U = 60$, ▲ $k_L = 60$ and $k_U = 120$, ▼ $k_L = 120$ and $k_U = 240$; (d) forced turbulence ····· full: ■ $k_L = 6$ and $k_U = 30$, ● $k_L = 30$ and $k_U = 70$, ▲ $k_L = 70$ and $k_U = 120$, ▼ $k_L = 120$ and $k_U = 240$.

For isotropic turbulence the log-normal distribution in figure 16(a) suggests and confirms the intermittent character of the fluctuating enstrophy. For inviscid flows the elongated tails with a less steep slope in figure 16(a) account for an increase of the probability of high values of $|\omega|$. By considering that $\langle\omega^2/2\rangle^{1/2}$ for the Lamb dipoles, the Taylor–Green flow and isotropic turbulence are 5.0, 1.8 and 16.0 respectively, the p.d.f. confirm that in a reasonably large number of points, high vorticity levels may occur. The flow visualizations in figures 11 and 12 revealed that the relevant structures are sheet-like; the p.d.f. of σ emphasize that vorticity amplification is not an isolated event. To see that the structures are thin curved ribbon-like, the visualizations are, however, necessary. For viscous flows the thin curved layers, while are generated, diffuse, and then the probability of high values of σ decreases.

The structure similarity was guessed by the energy spectra with wide power laws and it was observed by flow visualizations, which is confirmed through the p.d.f. of σ for the filtered fields. Figures 16(b) and 16(c) show that for the two inviscid flows the distributions do not change. For isotropic turbulence figure 16(d) demonstrates the absence of structure similarity. The filtered fields at the end of the dissipation range ($k_L = 120$, $k_U = 240$) give the anomalous curve in figure 16(d), which could be related to the insufficient resolution close to $k^* = 1$, causing the energy pile-up at $k^* = 1.2$ in figure 5(a).

The short log distribution of σ in figure 16(d) for the structures emerging from the energy spectrum in the range between $k_L = 6$ and $k_U = 30$ is a convincing demonstration that the viscosity reduces the vorticity intensity in the thin layers. In the range between $k_L = 30$ and $k_U = 70$, corresponding to the bump in the spectrum, the tail extends ($\langle \omega^2/2 \rangle^{1/2} = 10$ and $|\omega|_{max} = 158$). In the first part of the dissipation range the structures are more intermittent and the tail becomes wider for the decrease of $\langle \omega^2/2 \rangle^{1/2}$ to 7.2.

3.4. *Eigenvalues of the strain rate tensor*

A further quantitative picture of the shape of the structures is obtained by the eigenvalues of the strain rate tensor $\widetilde{S}_\lambda$, with $\widetilde{S}_3$ negative, $\widetilde{S}_1$ positive and the intermediate $\widetilde{S}_2$ either positive or negative. In turbulent flows, the number of points N_S with sheet-like structures ($\boldsymbol{R}_{\widetilde{S}} \leqslant 0$) is greater than the number N_R with rod-like structures ($\boldsymbol{R}_{\widetilde{S}} > 0$). For Lamb dipoles, counting all the points, 53 % accounts for $\boldsymbol{R}_{\widetilde{S}} \leqslant 0$; while by considering the points with vorticity amplification ($|\omega| > \Omega_T = 11$), the percentage of the locations with $\boldsymbol{R}_{\widetilde{S}} \leqslant 0$ increases to 60 %. It has also been found that the space where vorticity is amplified covers 4.6 % of the whole computational box. For the Taylor–Green flow $|\omega|$ is amplified ($|\omega| > \Omega_T = 1$) in 59 % of the points, that is, in a region greater than that for the Lamb dipoles. Figure 8(a) indeed shows that $|\omega|$ is amplified also in the elongated thin straight structures not relevant to produce the k^{-3} power law in the energy spectrum. In the locations with $|\omega| > \Omega_T$ the sheet-like structures prevail; in fact, N_S is 75 % of the points. For isotropic turbulence, the vorticity is uniformly distributed and then it is not important to impose a threshold value Ω_T to evaluate the locations of sheet-like structures. For this flow $\boldsymbol{R}_{\widetilde{S}} \leqslant 0$ in 71 % of the points.

From these arguments it can be concluded that ribbon-like structures are generated when the vortical structures interact inviscidly. For inviscid and for fully turbulent flows, the ribbon-like structures overcome the rod-like structures. The latter are responsible for the formation of the exponential range in the energy spectra; in fact, in isotropic turbulence, filtered with $k_L = 120$ and $k_U = 240$, N_S becomes equal to N_R.

3.5. *Enstrophy production*

The enstrophy production $\langle \omega_i \omega_j \boldsymbol{S}_{ij} \rangle$ is the term producing the vorticity amplification; for inviscid flows it is a measure of the formation of the small scales, where high vorticity is localized. In the principal axes the three terms of the enstrophy production $\langle \widetilde{\omega}_\lambda^2 \widetilde{S}_\lambda \rangle$ allow to understand which are the events contributing to the formation of the small scales with vorticity intensification.

In laminar and turbulent flows the vorticity vector tends to align with the intermediate strain $\widetilde{S}_2$; this $\widetilde{\omega}_2$ component is relevant to have information on the dynamics of the structures. For the interacting Lamb dipoles, Orlandi & Carnevale (2007) found that during the vorticity amplification, $\widetilde{S}_2$ is proportional to $\widetilde{\omega}_2$. This observation supports the idea that the $\widetilde{\omega}_2$ transport equation can be approximated to a one-dimensional model equation leading to FTS. If a proportionality between $\widetilde{S}_2$ and $\widetilde{\omega}_2$ indeed exists, these two quantities should contribute to the total enstrophy production, and consequently the sum of the other two terms is irrelevant. At high Reynolds number or in inviscid simulations the total enstrophy production is positive. Since $\widetilde{\omega}_1^2 \widetilde{S}_1 > 0$ and $\widetilde{\omega}_3^2 \widetilde{S}_3 < 0$ the intermediate component $\widetilde{\omega}_2^2 \widetilde{S}_2$ plays a relevant role. For a large number of events the mutual cancellation between $\widetilde{\omega}_1^2 \widetilde{S}_1$ and $\widetilde{\omega}_3^2 \widetilde{S}_3$ has been observed, and in addition it has been found that $\langle \widetilde{\omega}_1^2 \widetilde{S}_1 \rangle > -\langle \widetilde{\omega}_3^2 \widetilde{S}_3 \rangle$ and that $\langle \widetilde{\omega}_2^2 \widetilde{S}_2 \rangle$ prevails. Indeed the observations for inviscid flows are verified during the vorticity

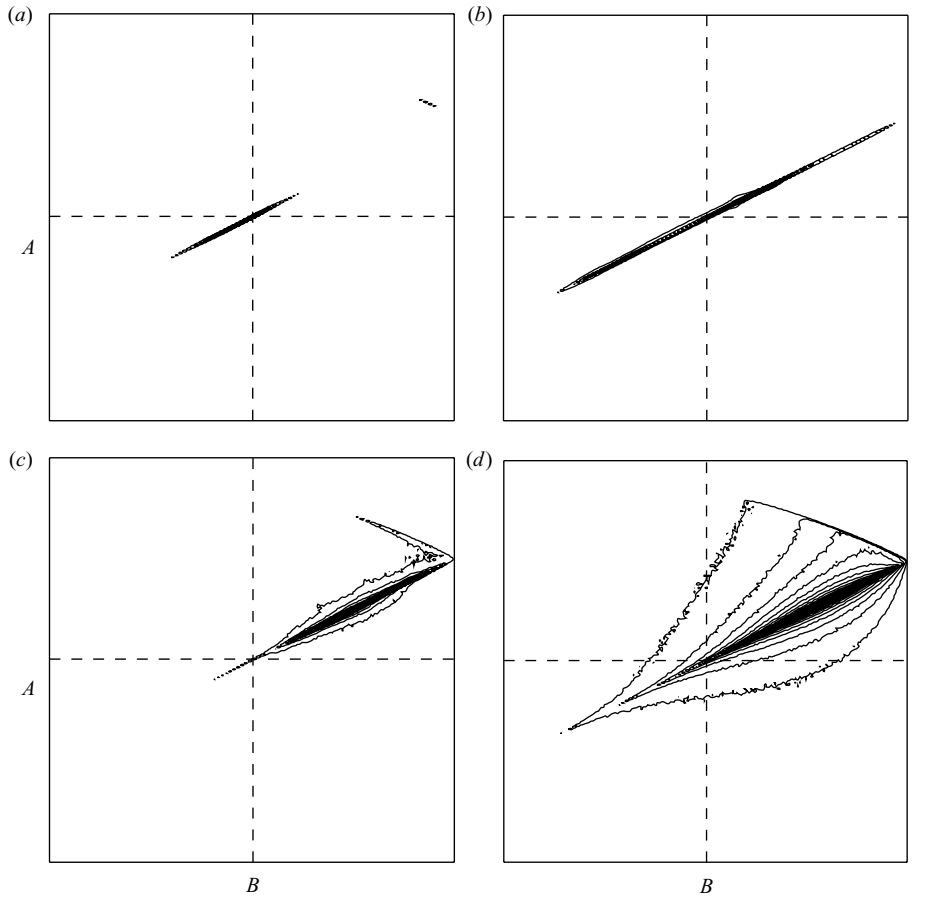

FIGURE 17. Joint p.d.f. of $A = \sqrt{6}\,\widetilde{S}_2/|S|$ (abscissa) and $B = \sqrt{1.5}\widetilde{\omega}_\lambda^2\widetilde{S}_\lambda/(|S||\omega|^2)$ (ordinate), both vary between -1 and $+1$, for (a) interacting Lamb dipoles at $t = 1$ $\Delta = 810^{-5}$, (b) at $t = 2.72$ $\Delta = 310^{-6}$, (c) Taylor–Green $t = 4$ $\Delta = 1.510^{-5}$ and (d) isotropic forced turbulence at $t = 7$ $\Delta = 410^{-6}$.

amplification. The values of $\alpha_\lambda = \langle\widetilde{\omega}_\lambda^2\widetilde{S}_\lambda\rangle/\langle\omega^2/2\rangle$ for the Taylor–Green flow at $t = 4.27$ for $\lambda = 1, 2$ and 3, respectively, are 0.66, 1.41 and -0.30. For the interacting Lamb dipoles, instants of high ($t = 2.72$, figure 7a) and low amplification ($t = 1$, figure 1b) have been considered. At low amplification rate ($t = 1$) the values of α_λ are 0.12, 0.0042 and -0.0297, and at high amplification rate ($t = 2.72$) they are 5.41, 7.99 and -4.14. These values support the cancellation and remark that the enstrophy production in large part comes from the component $\lambda = 2$. To demonstrate that the contribution to $\langle\widetilde{\omega}_2^2\widetilde{S}_2\rangle$ comes from ribbon-like structures (those with $\widetilde{S}_2 > 0$), the joint probability distributions between $A = \sqrt{6}\widetilde{S}_2/|S|$ and $B = \sqrt{1.5}\widetilde{\omega}_\lambda^2\widetilde{S}_\lambda/(|S||\omega|^2)$ have been evaluated ($|S| = (\boldsymbol{S}_{ij}\boldsymbol{S}_{ji})^{1/2}$). The normalization is made to deal with the absolute values of the coordinates not exceeding 1. The histogram of these two quantities were given by Kerr (1987) for isotropic turbulence, and it was not possible to understand the influence of $\widetilde{S}_2$ on the enstrophy production. The joint p.d.f. in figure 17(a) shows that at $t = 1$, before the vorticity amplification stage, the enstrophy production is small, and in particular because of $\widetilde{S}_2 \approx 0$. During the strong interaction between

the Lamb dipoles (figure 17*b*) there is a perfect correlation between A and B, and the events with positive $\widetilde{S}_2$ contribute most to the enstrophy production term. For the Taylor–Green flow (figure 17*c*) the correlation is reduced, and this reduction can be related to the formation of the thin straight vorticity layers discussed above. For this flow, figure 17(*c*) shows that quite high values of $\widetilde{S}_2$ are requested for the enstrophy production. Even if the previous arguments do not apply to viscous flows, figure 17(*d*) shows that the correlation is rather good.

4. Conclusions

By DNS any kind of quantity can be calculated and then any attempt to connect the shape of the vortical structures to the shape of the power laws is facilitated. In real flows, the viscosity produces at high wavenumbers (and also at very high Reynolds numbers) spectra with an exponential range. The small scales, therefore, affect the large scales, and in accord to the Kolmogorov theory, an inertial range with a $k^{-5/3}$ power law forms. Often it was speculated that a similarity between the energy cascade in turbulent flows and that in inviscid flows does exist. The DNS is the only way to deal with a true inviscid flow evolving from smooth initial conditions. In addition, these simulations could shed light on one of the most challenging open questions in fluid dynamics as to whether it is possible to find a convincing proof of the FTS for the Euler equations, and to analyse the influence of the initial conditions. This topic has been discussed only marginally in the present paper, in part because the author is convinced that a definite answer is impossible with the computer resources available today. From the theoretical speculation, at a time close to the hypothetical FTS (Kerr 1993), the energy spectra should display a k^{-3} decay; two inviscid simulations, with different initial conditions, allowed to find a time when the spectra approximate the k^{-3} power law for a wide range of wavenumbers. The grid refinement checks have demonstrated that the unphysical small scale structures related to the energy pile-up at high k do not affect the enstrophy-containing scales of interest. From these fields the statistics and the vorticity flow visualizations have been compared with those obtained in forced isotropic turbulence. It has been found that in the inviscid flows the k^{-3} is related to ribbon-like structures with small curvature radii near the location of maximum vorticity amplification. By filtering the velocities in k space it was shown that at each range of wavenumbers, the relevant structures are self-similar.

For isotropic turbulence in the inertial range, ribbon-like structures with mild curvature radii have been detected. At high R_λ at the end of the inertial range, a bump in the compensated spectrum is usually observed. By filtering the fields only within this range of wavenumbers, elongated rod-like structures are detected, which are surrounded by few ribbon-like structures. In the exponential range the latter disappear, and the rod-like structures become shorter and are isotropically oriented. The comparison between inviscid and viscous flows leads to the conclusion that the slope of the power law depends on the shape of the structures. The slope is mild when ribbon-like structures have large curvature radii and steep when the curvature radii are small.

The DNS allow to evaluate the rate of strain and of rotation tensors, however, it is difficult to relate the shape of the structures to them. The projection of the strain tensor components on the principal axes shows that the most relevant structures, those with $\widetilde{S}_2 > 0$, are ribbon-like. Among the three vorticity components the $\widetilde{\omega}_2$ accounts for $|\omega|$. It has been finally observed that intense vorticity amplification is linked to

strong enstrophy production, and in particular to $\widetilde{\omega}_2^2\widetilde{S}_2$, which prevails because of the proportionality between $\widetilde{S}_2$ and $\widetilde{\omega}_2$. For the inviscid interaction of two Lamb dipoles, during the vorticity amplification, a good correlation between $\widetilde{\omega}_\lambda^2\widetilde{S}_\lambda$ and $\widetilde{S}_2$ has been observed. This behaviour can be attributed to the persistence of a k^{-n} of the energy spectra during the interaction, with the exponent n varying continuously between $n=6$ and $n=3$. The correlation between $\widetilde{\omega}_\lambda^2\widetilde{S}_\lambda$ and $\widetilde{S}_2$ reduces for the Taylor–Green flow because the structures have a mild curvature during the evolution and the energy spectra at high k have a logarithmic decrement. The correlation between $\widetilde{\omega}_\lambda^2\widetilde{S}_\lambda$ and $\widetilde{S}_2$ reduces for forced isotropic turbulence for the presence of a large number of rod-like structures, those responsible for the exponential decay of $E(k)$ at high k.

The support of a MIUR 60 % grant is acknowledged. The computer time was given by CASPUR and by the San Diego Supercomputer Centre. Some of the simulations were performed in a cluster acquired through a PRIN grant. The continuous discussions with G. F. Carnevale were enlightening, and his comments on the first draft are acknowledged. For the revised version I have benefited from the discussions with S. Pirozzoli and the criticisms of the reviewers.

REFERENCES

Alvelius, K. 1999 Random forcing of three-dimensional homogeneous turbulence. *Phys. Fluids* **11**, 1880–1889.

Ashurst, W. T., Kerstein, A. R., Kerr, R. M. & Gibson, C. H. 1987 Alignment of vorticity and scalar gradient with strain rate in simulated Navier–Stokes turbulence. *Phys. Fluids* **30**, 2343–2353.

Burattini, P., Antonia, R. A. & Danaila, L. 2005 Similarity in the far field of a turbulent round jet. *Phys. Fluids* **17**, 025101.

Cichowlas, C. & Brachet, M. 2005 Evolution of complex singularities in KidaPelz and Taylor–Green inviscid flows. *Fluid Dyn. Res.* **36**, 239–248.

Cichowlas, C., Debbashn, F. & Brachet, M. 2006 Evolution of complex singularities and Kolmogorov scaling in truncated three-dimensional Euler flows. In *IUTAM Symposium on Elementary Vortices and Coherent Structures: Significance in Turbulence Dynamics*, pp. 319–328. Springer.

Crocco, L. & Orlandi, P. 1985 A transformation for the energy-transfer term in isotropic turbulence. *J. Fluid Mech.* **161**, 405–424.

Domaradzki, J. & Rogallo, R. S. 1990 Local energy transfer and nonlocal interactions in homogeneous, isotropic turbulence. *Phys. Fluids* A **2**, 413–426.

Duponcheel, M., Orlandi, P. & Winckelmans, G. 2008 Time-reversibility of the Euler equations as a benchmark for energy conserving schemes. *J. Comput. Phys.* **227**, 8736–8752.

Gotoh, T. Fukayama D., & Nakano, T. 2002 Velocity field statistics in homogeneous steady turbulence obtained using a high-resolution direct numerical simulation. *Phys. Fluids* **14** (3), 1065–1081.

Grafke, T., Homan, H., Dreher, J. & Grauer, R. 2007 Numerical simulations of possible finite time singularities in the incompressible Euler equations: comparison of numerical methods. ArXiv:0711.2284v1 physics.flu-dyn.

Holm, D. D. & Kerr, R. M. 2007 Helicity in the formation of turbulence. *Phys. Fluids* **19**, 025101.

Horiuti, K. & Fujisawa, Y. 2008 The multi-mode stretched spiral vortex in homogeneous isotropic turbulence. *J.* Fluid Mech. **595**, 341–366.

Horiuti, K. & Takagi, Y. 2005 Identification method for vortex sheet structures in turbulent flows. *Phys. Fluids* **17**, 121703.

Hou, T. Y. & Li, R. 2006 Dynamic depletion of vortex stretching and non-blowup of the 3-D incompressible Euler equations. *J. Nonlinear Sci.* **16**, 639–664.

Ishihara, T., Kaneda, Y., Yokokawa, M., Itakura, K. & Uno, A. 2005 Energy spectrum in the near dissipation range of high resolution direct numerical simulation of turbulence. *J. Phys. Soc. Jpn* **74**, 1464–1471.

Ishihara, T., Kaneda, Y., Yokokawa, M., Itakura, K. & Uno, A. 2007 Small-scale statistics in high-resolution direct numerical simulation of turbulence: Reynolds number dependence of one-point velocity gradient statistics. *J. Fluid Mech.* **592**, 335–366.

Jimenez, J., Wray, A. A., Saffman, P. G. & Rogallo, R. S. 1993 The structure of intense vorticity in isotropic turbulence. *J. Fluid Mech.* **255**, 65–90.

Kaneda, Y. Ishihara T., Yokokawa, M. Itakura, K. & Uno, A. 2003 Energy dissipation rate and energy spectrum in high resolution direct numerical simulations of turbulence in a periodic box. *Phys. Fluids* **15**, L21.

Kerr, R. M. 1987 Histograms of helicity and strain in numerical turbulence. *Phys. Rev. Lett.* **59**, 783–786.

Kerr, R. M. 1993 Evidence for a singularity of the three-dimensional, incompressible Euler equations. *Phys. Fluids* A **5**, 1725–1746.

Kolmogorov, A. N. 1941 [1991] The local structure of turbulence in incompressible viscous fluid for very large Reynolds numbers. *Dokl Akad. Nauk SSSR* **30**, 301–305. English translation in *Proc. R. Soc. Lond.* A **434**, 9–13.

Lamb, H. 1932 *Hydrodynamics*. Cambridge University Press.

Moisy, F., & Jimenez, J. 2004 Geometry and clustering of intense structures in isotropic turbulence. *J. Fluid Mech.* **513**, 111–133.

Mydlarski, L. & Warhaft, Z. 1996 On the onset of high-Reynolds-number grid-generated wind tunnel turbulence. *J. Fluid Mech.* **320**, 331–368.

Orlandi, P. 2000. *Fluid Flow Phenomena: A Numerical Toolkit*. Kluwer Academic Publishers.

Orlandi, P., & Carnevale, G. F. 2007 Nonlinear amplification of vorticity in inviscid interaction of orthogonal Lamb dipoles. *Phys. Fluids* **19** (5), 057106.

Paczuski, M. & Bak, P. 1999 Self-organization of complex systems. ArXiv: cond-mat/9906077.

Saddoughi, S. G. & Veeravalli, S. V. 1994 Local isotropy in turbulent boundary layers at high Reynolds number. *J. Fluid Mech.* **268**, 333–372.

She, Z. S., Jackson, E. & Orszag, S. A. 1991 Structure and dynamics of homogeneous turbulence:models and simulations. *Proc. R. Soc. Lond.* A **434**, 101–124.

Vincent, A. & Meneguzzi, M. 1991 The spatial structure and statistical properties of homogeneous turbulence. *J. Fluid Mech.* **225**, 1–20.